Received: 28 January 2022 | Revised: 13 October 2022 | Accepted: 28 November 2022

DOI: 10.1002/we.2801

RESEARCH ARTICLE

WILEY

A CFD-based analysis of dynamic induction techniques for wind farm control applications

Alessandro Croce | Stefano Cacciola | Mariana Montero Montenegro | Sebastiano Stipa | Roberto Praticó

Dipartimento di Scienze e Tecnologie Aerospaziali, Politecnico di Milano, Milano, Italy

Correspondence
Alessandro Croce, Dipartimento di Scienze e Tecnologie Aerospaziali, Politecnico di Milano, Milano, Italy.
Email: alessandro.croce@polimi.it

Present address
Alessandro Croce, Dipartimento di Scienze e Tecnologie Aerospaziali, Via La Masa 34, Milano, 20156, Italy.

Funding information
This paper is part of the EU project FLOAWER: This project has received funding from the European Union's Horizon H2020 research and innovation programme under the Marie Słodowska-Curie grant agreement N° 860579.

Summary

Recently, dynamic induction control is gaining the interest of the wind energy community as a promising strategy to increase the overall wind farm power production. Such a technique is based on a dynamic variation of the upstream rotor thrust, generated through a suitable blade pitch motion, to promote a faster wake recovery. Notwithstanding some promising results already published, the knowledge of the physical mechanism, connecting dynamic induction to the increased in-wake velocity, was not yet exploited to enhance control effectiveness. This paper, through a computational fluid dynamics procedure based on large eddy simulations coupled with actuator line models, provides a description of the working principles of this control from a fluid dynamics standpoint. The analyses show that the faster recovery is strictly connected to the ability of the blade tip vortices to roll up and sucking energy from the outer flow. Exploiting such knowledge, a novel control strategy, which improves the vortex roll up mechanism, is proposed and analyzed. The new control proved more effective than standard techniques especially for very low turbine spacing.

KEYWORDS
active wake control, dynamic induction control, large eddy simulation, wind farm control

1 | INTRODUCTION

Aerodynamic and atmospheric phenomena that occur within large wind farms heavily influence the performance of individual wind turbines and, more specifically, can reduce the energy yield of the farm. It was estimated that overall farm power output is typically overestimated by 5% or more,[1] and among the many factors determining this gap, wake losses represent a significant source.

In order to reduce rotor–wake interactions, typically detrimental in terms of power and loading of downstream rotors, the synergistic control of all turbines belonging to a single farm, known as *wind farm control*, was studied and developed up to the first field experiences.[2] At present, all different wind farm controls, developed in the last decade, may be grouped in three main categories, on the basis of the technique adopted to cope with turbine–wake interactions: wake steering (WR) (see Fleming et al. (2019),[2] Gebraad et al. (2016),[3] and references therein), steady axial induction (see Annoni et al[4]), and dynamic induction control (DIC) (see Munters & Meyers (2017)[5]).

While WR is perhaps recognized as the most promising methodology, in recent years, the attention of the wind energy international community has been also put to the latter strategy. DIC technique, also called active wake mixing (AWM), is based on a cyclic variation of rotor thrust, which, through a complex fluid dynamics mechanism, has the effect of promoting a faster wake recovery. The wake of a machine operating with DIC results to be characterized by a higher mean velocity, which leads to an increase in the power produced by a downstream machine inside that wake.

The idea of increasing the power of a farm by dynamically varying the energy extraction of the single turbines dates back to the work of Goit and Meyers (2015).[6] In that paper, thanks to a large eddy simulation (LES) study, it was possible to prove that this technique is able to influence the flow within a very large wind farm and modify the vertical energy transportation so as to increase the overall production up to 16% in a single wind condition. Within this work, the turbine was considered as a simple flow actuator while the control was synthesized according to a receding-horizon technique (RHC). The work was then further re-elaborated in subsequent studies,[5,7,8] where promising results have been obtained also for smaller farms.

In particular, Yilmaz and Meyers (2017)[8] provide for a description of the working principles of DIC from a fluid dynamics standpoint, using LES simulations coupled with an actuator line-based model of the turbines and a synthetic generation of turbulence.[9] The authors showed how the dynamic variation of the rotor induction affects the evolution of the three vortex rings released by the blade tips, which interact and merge together, increasing the entrainment of momentum into the wake from the outer flow.

Finally, the extension of the algorithm to include dynamically varying yaw angle in the control has been presented by Munters and Meyers (2018).[10]

With the aim of simplifying the complexity and the computational burden of RHC, an alternative DIC based on a simpler predefined sinusoidal variation of the turbine axial induction factor was proposed.[11] The findings of this study are manifold. At first, it was shown that with this simpler strategy power, increments up to 5% are achievable using DIC only on the first upstream row of turbines belonging to a 4×4 farm. Moreover, the frequency and amplitude of the induction variation strongly affect the effectiveness of the control. The optimal frequency was found through a sensitivity study and qualitatively identified as the one at which the vortex rings are shed from the turbines. Consequently, it is expected that, rather than being influenced by the absolute value of the frequency, the DIC mechanism is related to the Strouhal number, defined as the frequency made dimensionless through the ratio between rotor diameter and wind speed.

Additional studies have followed the work of Munters and Meyers (2018).[11] First, an experimentation in wind tunnel has been conducted to validate DIC in a three-turbine scaled farm.[12] Variation of thrust and induction factor was obtained by a practical periodic collective motion (PCM) of the blade pitch angles. The study showed a possible increase in the overall power up to 4%, obtained at slightly different amplitude and Strouhal values with respect to the optimal ones found by Munters and Meyers (2018).[11] The same paper dealt with the first evaluation of the impact of DIC on turbine fatigue loads, showing a mild increase (less than 1%) in the fatigue of the blade of the upstream turbine generating DIC. A subsequent study also evaluated the impact of DIC in terms of ultimate loads, which were found to be of a similar magnitude with respect to the ones related to WR control (see Croce et al. (2022)[13]).

A comparison between the wind tunnel tests object of Frederik et al. (2020)[12] and LES simulations was presented by Wang et al. (2020),[14] where the LES environment was coupled with an actuator line model (ALM) to render turbine aerodynamics. The agreement, in terms of overall farm power, was rather good, especially in the vicinity of the optimal Strouhal number. The aeroelastic behavior of a turbine inside the wake shed by an upstream turbine operating with DIC was preliminary studied in Cacciola et al.(2020),[15] again in a LES-ALM environment. In this work, it was demonstrated that, in case DIC is active, the wake is characterized by a periodic "pulsating" wake that strongly interacts with the aeroservoelastic response of the downstream turbines.

Finally, through a LES-ALM simulation campaign, it was demonstrated that AWM can be generated also by a dynamic individual pitch of the blade, defined to mainly modify the direction of the thrust instead of its module.[16,17] The control was called "helix approach" because the resulting wake is characterized by bubbles of higher flow velocity which propagate downstream following a helical path. This control provides for a faster wake recovery with limited variation of the thrust magnitude, which could imply a lower impact on machine loading.

From the literature review, it is evident that DIC techniques are being developed but, while much has been actually achieved in few years, there is still much more we must study to clarify the overall performance of this control and understand whether it could flank the already established WR technique for present and future wind farm control strategies.

Even though Yilmaz and Meyers explained the working principle of DIC,[8] it is still not clear if and how this mechanism could be enhanced through a different set of controls.

The present paper, through a LES-ALM procedure, is aimed at finding a way to enhance the fluid mechanism underlying the DIC working principles. A first analysis on the evolution of the wake subject to DIC confirms the interpretation of the DIC working principles provided by Yilmaz and Meyers,[8] also in a slightly different scenario comprising a LES-computed turbulence (not synthetic) and a DIC based on a simple PCM. In particular, the active mixing is mainly due to the interaction between the blade tip vortices and the outer flow. In the case of PCM, the vorticity released in the flow is variable following the periodicity of the thrust and the rotor induction. As a consequence, the topology of the wake shows up with alternating rings of high and low vorticity, which tend to last longer. In this situation, the boundary layer easily rolls around the higher vorticity cores, a phenomenon often called vortex roll up. The additional suck of energy from the outer flow induced by the vortex roll up is mostly responsible for the faster recovery in the wake. Obviously, influencing this mechanism in the correct way may lead to an improved DIC strategy.

To this end, two DIC techniques, tailored for improving the vortex roll up mechanism, are proposed as alternatives to the standard PCM based on sinusoidal functions. The first one, called Gaussian PCM (GPCM), is based on an asymmetric periodic pitch motion, defined through Gaussian functions. While maintaining a zero mean pitch variation, the GPCM function is characterized by a high pitch maximum, opportunely defined to reduce the angles of attack of the blade sections in a particular instant of time, to almost annihilate the magnitude of the low-vorticity cores. The second technique is based on a periodic deflection of the blade tip, called tip PCM (TPCM), envisioned with the scope of acting directly on the location where the vorticity is released, with a lower expected impact on blade loading.

Only the first technique resulted effective to improve the DIC process. In fact, with GPCM the vortex roll up occurs closer to the rotor disk, providing a significant contribution to the wake re-energization already from a downstream distance of 1.5 diameters. On the contrary, the TPCM has not enough energy to create significant changes in the vorticity generated by the whole rotor and, hence, is not able to trigger a faster recovery.

The results obtained with the GPCM control, besides demonstrating the effectiveness of the novel strategy, prove also that the DIC working principles were correctly interpreted.

The paper is written according to the following plan. Section 2 presents the computational fluid dynamics (CFD) environment focusing on the tools used in the analysis and the description of the different DIC strategies. Section 3 deals with the analysis of the DIC working principles providing a thorough description of the impact of such control on blade tip vortices and the flow within the wake. Section 4 reports the results of two sets of simulations, with a single and two aligned turbines, used for quantifying the impact of these DIC strategies in terms of in-wake mean flow velocity and produced power. Finally, Section 5 finalizes the manuscript summarizing the main findings of this research.

2 | COMPUTATIONAL FLUID DYNAMICS ENVIRONMENT

2.1 | Tools of analysis

The CFD environment adopted in this work for simulating and analyzing the flow within a wind farm is based on an unstructured colocated LES solver within the OpenFOAM (Open Field Operation And Manipulation) framework. In order to model the presence of the turbine in the CFD environment, OpenFOAM is coupled with OpenFAST (Open Fatigue Aerodynamics Structures and Turbulence),[18] an aero-servo-elastic tool implementing the ALM to render the rotor aerodynamics. The communication between the two solvers, fluid and turbine dynamics, and the time marching of the simulation are handled by a software developed by NREL (National Renewable Energy Laboratory) named SOWFA (Simulator fOr Wind Farm Applications),[19] which represents a plugin to the original OpenFOAM-2.4.x release and includes new solvers and libraries specifically conceived for wind energy purposes. The fluid dynamics model is based on the filtered incompressible Navier–Stokes equations with Coriolis force and buoyancy, where the latter is modeled using the Boussinesq approximation. Finally, the aerodynamics of the turbines is rendered through the classical ALM. Accordingly, each blade is viewed as a collection of several airfoils, distributed along its span. The aerodynamic properties of all airfoils, that is, lift, drag, and moment coefficients, are given as tabulated functions of the angle of attack and, possibly, Reynolds number. The flow velocity vector along the blade span is sampled from the LES grid and then fed to the lifting lines yielding the distributions of lift, drag, and moment, which are then projected back onto the LES grid as a body force field, using the isotropic Gaussian projection function.[20]

Within SOWFA, the two-step analyses, based on *precursor* and *successor* simulations, can be employed for replicating *in silico* wind turbine operations under turbulent wind conditions.

In particular, during the precursor run, a turbulent flow of specific characteristics is generated within an empty domain, that is, without turbines. Precursor simulations require a careful analysis of turbulence statistics convergence in order to assess the correctness of the generated turbulent fields (see Section 2.2). Once the atmospheric boundary layer has developed, the inlet boundary conditions are recorded at each time step and then used as inflow boundary conditions for the successor simulations, in which one or more turbines are inserted.

Both tools of wind farm and turbine analysis, SOWFA and OpenFAST, have been installed on the high-performance computers managed by the SCAI (SuperComputing Applications and Innovation) department of the Italian inter-university consortium CINECA.[21] On those machines, a 30,000-s precursor simulation with 9 million cells is run for about 24 h wall time using 408 cores, while an 800-s successor simulation having two wind turbines with 12.4 million cells is run for about 8 h using 324 cores.

2.2 | Precursor simulations and boundary layer analysis

In the present section, the precursor simulations, used for generating realistic atmospheric boundary layers (ABLs), are presented and analyzed.

Within the development of this work, only neutral atmospheric boundary layers have been considered. Accordingly, different values of the equivalent roughness length z_0 have been selected to obtain flows with different turbulence intensity levels.

In all simulations, the velocity is controlled through a uniform pressure gradient, adjusted at each iteration, to obtain a wind speed of 9 m/s at a reference height of 90 m (equal to the turbine hub height; see Section 2.3.2). Such a wind speed has been selected as a generic velocity for which a wind farm control is supposed to be active and effective for power harvesting maximization. Precursor simulations are initialized using a logarithmic wind profile, while potential temperature is set according to the model proposed in Rampanelli and Zardi,[22] using a capping inversion width of 100 m, a reference potential temperature of 300 K, an initial capping inversion height of 750 m, a potential temperature jump across the capping inversion of 5 K and a stable lapse rate of 3 k/km. Turbulence is triggered using sinusoidal spanwise velocity perturbations in the first 100 m of the ABL. The Coriolis parameter is set to 4.813e-5 rad/s, corresponding to a latitude of 41.44°. As turbulence is developed inside the ABL, the velocity controller slowly rotates the wind direction at geostrophic height, trying to maintain the desired magnitude and direction at the reference height. After 20000 s of model time, the ABL height becomes constant as the simulation progresses, and turbulence statistics can be collected. After this initial spin-up phase, velocity, potential temperature, and subgrid kinetic energy are recorded for 1000 s on a slice normal to the streamwise direction at hub height. Such 'inflow database' will be later used as inflow condition for successor simulations. In Table 1, equivalent roughness values, resulting turbulence intensity levels at 90 m and shear exponents obtained by fitting an exponential law to the LES wind profile between 0.2 and 2 hub heights, are reported. Clearly, the higher the roughness coefficient, the higher the turbulence and the shear of the wind profile.

Both precursor and successor domains are cuboids of dimensions $3 \times 3 \times 1$km (length×breadth×height). In order to ensure the best possible accuracy of the LES procedure, while maintaining low computational costs, the grid size has been set in accordance to Brasseur and Wei criteria.[23] In fact, given the estimated value for the viscous Reynolds Re_τ of about $17.5 \cdot 10^6$, a complete resolution of the surface layer would not be feasible, but good law of the wall agreement in the inertial range can be achieved. By using a grid resolution of 10x10x10 m (length × breadth × height) it was possible to bury the spurious overshoot in the shear profile, resulting from LES-dependent length scales, inside the first cell. Classic periodic boundary conditions on vertical patches are adopted. On the upper patch, a specified normal gradient - equal to the lapse rate above the inversion - is used for temperature, while slip condition is used for velocity. On the bottom patch, velocity is set so that the normal gradient at the wall matches the one calculated at the first internal cell. At the same time, the sub-grid viscosity is set to zero at the wall, so that viscous fluxes do not contribute to the wall shear stress. Instead, the latter is evaluated through the Shumann model[24] and its contribution to the momentum equation is explicitly added when evaluating viscous fluxes at the wall faces to match the law of the wall locally. Finally, a zero-gradient boundary condition is used for the potential temperature as the latter is constant below the inversion layer. To evaluate subgrid stresses, we adopt the model proposed by Moeng,[25] that is, a one-equation model for the kinetic energy of the subgrid-scale motions, which includes stability corrections and is already built-in within SOWFA. Using a differential model allows for larger time steps and nonequilibrium conditions. Moreover, the model constant C_k, appearing in computation of the subgrid-scale viscosity $\nu_k = C_k V^{3/4}\sqrt{k}$, with V the local cell volume and k the turbulent kinetic energy, has been tuned in order to optimally capture law-of-the-wall scaling in the inertial range. After a trial-and-error approach, a value of $C_k = 0.087325$ appeared to yield the best matching for all considered scenarios. For all three precursor cases, it was verified that the obtained ABLs satisfied the expected theoretical behavior. In particular, Figure 1 shows, on the left, the dimensionless flow velocity, u/u_τ, being u the longitudinal velocity and u_τ the friction velocity, as a function of the vertical distance from the bottom patch. The black solid line represents the theoretical logarithmic law of the wall, given by

$$u(z) = \frac{u_\tau}{\kappa} ln\left(\frac{z}{z_0}\right) \tag{1}$$

where we used $\kappa = 0.41$. In the same figure, on the right, the dimensionless derivative of Equation (1), namely $\frac{du}{dz}\frac{\kappa z}{u_\tau}$, it is shown as function of the vertical distance from the bottom patch. Such variable should approach a unitary value in the inertial range for null heat flux at the ground.[26] Despite some small deviations from the theoretical logarithmic law at the first cell center (Figure 1A), an acceptable law-of-the-wall agreement is obtained and the spurious overshoot described by Brasseur and Wei (2010)[23] is not present in the nondimensional shear profile. Moreover, the deviation at the first cell center is due to the dummy velocity boundary condition explained above, needed by OpenFOAM to compute velocity gradients. We emphasize that the latter does not affect the wall shear stress, as viscous fluxes are explicitly set at the wall through the Shumann model.

TABLE 1 Precursor data: Roughness length z_0, turbulence intensity and vertical shear layer

ID	z_0 (m)	TI (%)	Vertical shear
P-Z003	0.003	5.02	0.107
P-Z030	0.030	6.35	0.137
P-Z150	0.150	7.61	0.174

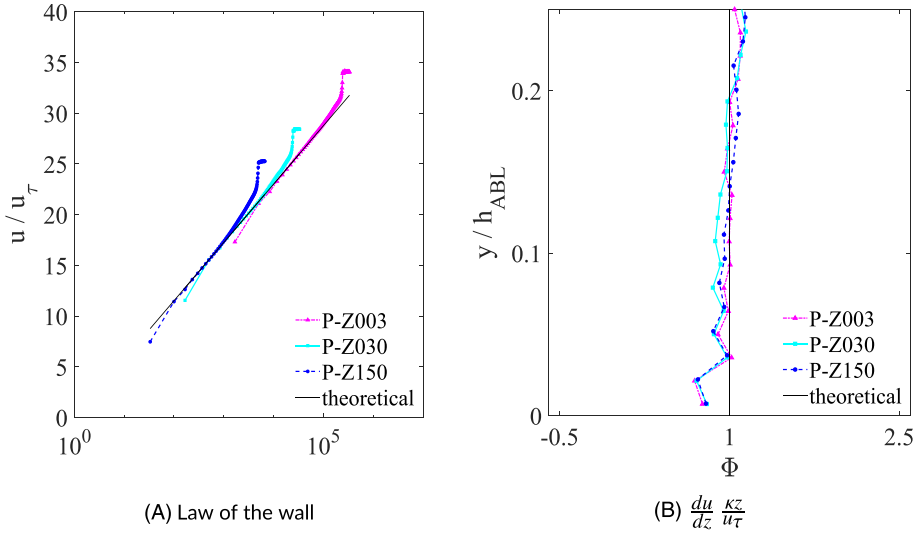

(A) Law of the wall

(B) $\frac{du}{dz}\frac{\kappa z}{u_\tau}$

FIGURE 1 (A, B) Law-of-the-wall scaling of ABL simulations

In order to assess if the domain was large enough to ensure that no turbulent eddies were exchanged from the outlet back to the inlet due to periodic boundary conditions, correlation analyses have been carried out. Specifically, acquisition probes were inserted in the domain to measure velocity along streamwise and spanwise lines at different heights. We found eddy life scale to be less than the flow through time at hub height, allowing sufficient velocity decorrelation. This scale can be calculated by looking at the integral of the slowest-decreasing correlation along a space-time direction, that is, following the eddy along its motion. Kolmogrov $-5/3$ scaling was also assessed by computing wave-number spectra of velocity correlations. For the sake of brevity, results from the latter two studies are not reported in the manuscript. To conclude, considering that we followed NREL guidelines on using SOWFA, that logarithmic, nondimensional shear scalings and spectra showed close to theoretical behaviors, we are confident that our precursor runs represent an accurate inflow for our successor simulations.

2.3 | Successor simulations through coupled CFD-multibody simulations with DIC

2.3.1 | Successor definitions

Successor analyses share with the precursor simulations the same domain and the same boundary conditions for all patches but the inlet and outlet ones. Velocity, temperature, and turbulent kinetic energy in the inlet patch were mapped from the precursor results, whereas in the outlet one, zero-gradient boundary condition is used for temperature and turbulent energy, while velocity is set to zero-gradient if exiting the domain and zero if entering the domain. Two levels of mesh refinement have been used for having a resolution of 2.5 m where the turbines are located and where their wake develop. Note that, since these refinements do not intersect the inlet, the precursor and the successor meshes are consistent here, and mapping the inflow database does not require any interpolation.

2.3.2 | Reference wind turbine model and two-turbine wind farm layout

The wind turbine model adopted in all wind plant simulations is the "NREL 5-MW Baseline".[27] The model represents a realistic conventional three-bladed, upwind, variable speed, and variable blade pitch controlled turbine. The turbine has a diameter of 126 m and hub height equal to 90 m. Cut-in and cut-out wind speeds are, respectively, equal to 3 and 25 m/s, whereas the rated power of 5 MW is reached at the rated wind speed of 11.4 m/s. Finally, rated rotor speed is equal to 12.1 RPM.

Both isolated turbine and simple two-turbine wind farm simulations have been considered in this work. For the first set of simulations, a turbine model is located at 1500 m from the west patch in the middle of the domain. For the cases related to wind farm analyses, a second turbine is added downstream, so as the two turbines are aligned to the flow direction. Two different spacing, that is, 3 and 5 diameters, are analyzed.

2.3.3 | DIC techniques

The controller of the machine, based on classical PID regulators, provided within the turbine model, was modified to consider the possibility to generate the DIC through a periodic collective pitch motion (PCM). Three types of PCM strategies are considered.

The first is based on a standard sinusoidal pitch motion called hereafter SPCM, to be added to the trimmer input, as follows:

$$\beta_{\text{coll}} = \beta_{\text{trim}} + \beta_{\text{SPCM}} \sin(2\pi f_{\text{SPCM}} t + \phi_{\text{SPCM}}), \tag{2}$$

where β_{coll} is the blade collective pitch setting, β_{trim} is the pitch angle imposed by the trimmer (i.e., the standard pitch-torque turbine regulator), and t is the simulation time, whereas β_{SPCM} and f_{SPCM} are, respectively, the amplitude and the frequency set for PCM. Finally, $\phi_{\text{SPCM}} = -2\pi f_{\text{SPCM}} t_0$ is the phase of SPCM oscillation used to avoid discontinuity in blade pitch demand at the instant t_0 of SPCM activation.

The PCM frequency is typically expressed through the dimensionless Strouhal number defined as $S_t = (f_{SPCM} D)/U$, where U is the undisturbed wind speed.

Clearly, within the oscillation period, the blade pitch angle changes in a symmetric way with respect to its mean value, entailing an almost symmetrical (sinusoidal) modulation of both the blade section angles of attack and the rotor thrust.

After a deep analysis of wake flow and tip vortex development, which will be detailed in Section 3, it was observed that a nonsymmetric pitch variation, with increased values of positive pitch angles and, hence, lower value of angles of attack at blade sections, is beneficial for improving the mixing phenomena and, hence, increasing the effectiveness of the PCM strategy.

To this end, in this work a second kind of PCM control is considered, which is based on a combination of Gaussian functions set so as to have a periodic motion with a non symmetric oscillation around the zero mean.

This strategy, indicated with GPCM, gives the following pitch actuation:

$$\beta_{\text{coll}} = \beta_{\text{trim}} + \beta_{\text{GPCM}} k(\tau), \tag{3}$$

where β_{GPCM} is the amplitude of the GPCM control, evaluated starting from the SPCM amplitude as $\beta_{\text{GPCM}} = \beta_{\text{SPCM}} / \min(k(\tau))$.

The nondimensional variable $k(\tau)$, function of a generic non-dimensional time parameter $\tau \in [0,1]$, is

$$k(\tau) = (G1(\tau) + G2(\tau) + B)\sin^{\xi}(\pi\tau), \tag{4}$$

where the two Gaussian function $G1$ and $G2$ are

$$\begin{aligned} G1(\tau) &= -\frac{1}{s_1\sqrt{2\pi}}\exp\left(-0.5\left(\frac{\tau - m_1}{s_1}\right)^2\right) \\ G2(\tau) &= +\frac{1}{s_2\sqrt{2\pi}}\exp\left(-0.5\left(\frac{\tau - m_2}{s_2}\right)^2\right), \end{aligned} \tag{5}$$

with

$$s_1 = \frac{p}{2\sigma(1+p)},\ s_2 = \frac{1}{2\sigma(1+p)},\ m_1 = \frac{p}{2(1+p)} \text{ and } m_2 = \frac{2p+1}{2(1+p)}. \tag{6}$$

B,ξ,p, and σ are all nondimensional parameters to be defined so as to have a desired asymmetric function. In particular, the parameter p is the ratio between the periods of the Gaussian functions $p = T_{G1}/T_{G2}$,σ is the ratio between the Gaussian period and its standard deviation (equal for both $G1$ and $G2$), and B is chosen so as to have the minimum GPCM pitch value equal to the SPCM one. Finally, to transform function k into a periodic one with a specific period T_{SPCM}, one has to set

$$\tau = \frac{t}{T_{SPCM}} - \text{floor}\left(\frac{t}{T_{SPCM}}\right). \tag{7}$$

As an example of these parameters, Figure 2 shows a comparison between the SPCM and GPCM pitch motion, in case the following parameters are set: $\beta_{\text{SPCM}} = 2.5^\circ$,$f_{\text{SPCM}} = 0.0259\,\text{rad/s}$,$C = 0.222$,$p = 8$,$\sigma = 0.5$,$\xi = 2$, and $T_{SPCM} = 1/f_{\text{SPCM}} = 38.67$. To better show the difference of the two signals, in Figure 2, the SPCM signal is offset by half a period.

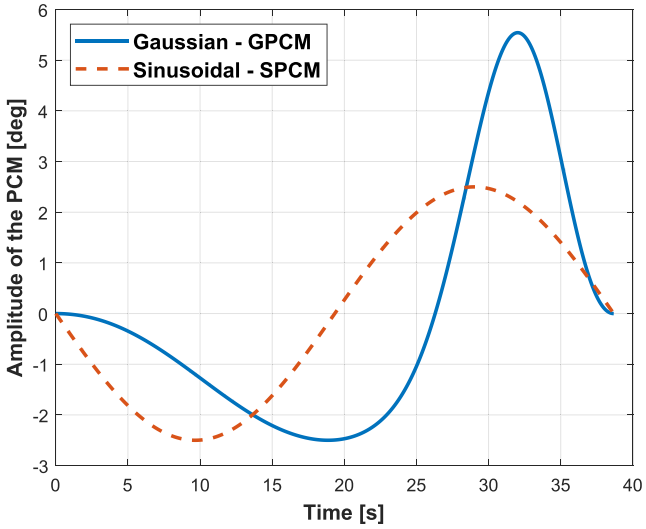

FIGURE 2 Pitch motion entailed by standard sinusoidal pitch motion (SPCM) (dashed line) and Gaussian PCM (GPCM) (solid line) within one control period

Notice that, besides having the same period and hence the same associated Strouhal number, the two functions share the same minimum value, meaning that the blades will experience a similar increase in the sectional angles of attack. On the contrary, the GPCM strategy entails a higher variation of the pitch, which are associated to a lower thrust than the one of the SPCM.

In a third analyzed strategy, only the last 10% of the blades moves according the SPCM strategy. This strategy, which will be named hereafter tip PCM or TPCM, is inspired by the fact that the mixing mechanism is strongly influenced by the tip vortices. To this end, it could be expected that acting only in the region where the tip vortices generate and develop, one could trigger the AWM mechanism, without penalizing too much the blade loads. In this case, the tip of the blade, assumed to be movable, is controlled according to a purely sinusoidal motion as in Equation (2).

3 | ANALYSIS OF THE PHYSICS OF DIC

In the present section, the development of a wake generated by a turbine operating with DIC is investigated. The aim of this section is to understand whether the fluid dynamic mechanism of DIC can be enhanced by a proper selection of the control function. A similar analysis was already carried out by Yilmaz and Meyers.[8] Our analysis, from the one hand, confirms Yilmaz's and Meyers's interpretation and from the other extends their treatment showing a way to boost the fluid dynamic mechanism underlying DIC.

In fact, it will be pointed out how the shape of the control law can impact the different features of the flow in the turbine wake, justifying the interest in asymmetrical Gaussian (GPCM) and tip PCM (TPCM) control functions as alternatives to sinusoidal PCM (SPCM).

A key aspect for comprehending the impact of DIC on the evolution of a wake is the vortex pairing mechanism, consisting in the coupling between two vortices, which roll around each other, coalesce and form a new bigger vortex. The strong impact of vortex pairing on the wake evolution is mainly due to the fact that this phenomenon triggers the transition between the near and the far wake.[28–30]

Before the blade tip vortices pair, the distribution of vorticity is coherent and organized in those helical vortex filament created by the motion of the blades. As claimed by Medici (2005),[31] such structures isolate the wake from the outer flow because the vortex filaments are close one to each other and do not have sufficient spatial separation to induce a radial flow velocity. As shown by Lignarolo at al (2004),[28] in the far wake, the vortex leapfrogging mechanism creates spatially separated high vorticity zones with short lifetime, which subsequently breaks up into small-scale turbulence, enabling the *momentum entrainment* from the outer flow.

Clearly, the wake re-energization process takes place only after the vortex pairing, when the outer flow can be sucked inside the wake, increasing its mean kinetic energy. This process is driven by the small-scale turbulence, whereas the pre-existent ABL turbulence has a strong influence on the position at which the instability of vortices occurs.[29,30]

3.1 | Impact of periodic collective blade pitch motion on near wake vortices

The previously highlighted mechanism suggests that an improved wake re-energization can be obtained by entraining momentum in the near wake as well. Since this region is shielded from the outer flow by the tip vortices, an early breaking of these structures could anticipate the

entrainment process. Moreover, being able to generate sufficiently spaced vortices immediately behind the rotor would allow induction phenomena on the surrounding flow, enabling an active mixing mechanism due to coherent vortex structures rather than small-scale turbulence only.

Periodically varying aerodynamic force distribution along the blades, for example, through a periodic pitching motion, generates an oscillation of the circulation around the blade and, hence, in the local vorticity magnitude. At this point, the presence of regions of with different vorticities allows an additional mixing through the overall roll up of the shear layer around the position of maximum vorticity. It should be noted that this process is different from the conventional leapfrogging, where all tip vortices have the same intensity and pairing happens between two of them, triggered by their mutual interaction.[32]

The vorticity dynamics inside the wake, as previously explained, can be observed in Figure 3 which shows the vorticity field inside a wake of a single wind turbine for a wind condition with 9m/s speed and 5% turbulence intensity (see ID P-Z003 in Table 1). Both sinusoidal PCM (left) and baseline (right), that is, without PCM, cases are considered. The plot represents different time shots of the vorticity in a horizontal slice at hub height, every 5 s for a total 35 s corresponding to about one PCM period. The pitch setting related to the SPCM strategy is the one described in Figure 2. Gray vertical lines indicate downstream distances equal to multiple of the rotor diameters.

As can be noticed, the tip vortices last longer time in the baseline case and, after their instability at 2 diameters, a weak vorticity-containing structure is formed, which finally breaks up in a noncoherent vorticity pattern around 3 diameters. After that point, the in-wake mixing is due only to the small-scale turbulence.

In the SPCM case, a large vortex has rolled up at 2.5 diameters (see second 700) and appears to have a lifetime of more than 5 diameters downstream, as denoted by the blue and red dots indicating the negative and positive vortex cores, respectively. Such big vortices, through the roll up of the shear layer, provide an additional contribution to the mixing entailed by small-scale turbulence.

Moreover, for the same condition, in Figure 4, a comparison related to the streamwise velocity component is displayed. The plot is organized as in Figure 3, with the left part showing the SPCM case and the right one the baseline. In the left part, blue and red dots are also reported to indicate the position of the cores of the vortices as detected in Figure 3.

Two effects are clearly visible. The first one is the higher level of mixing characterizing the SPCM case over the baseline one, which generates a higher in-wake velocity. Notice also how a strong mixing starts 2.5 diameters downstream, as an effect of the coherent PCM vortices. The second one is the fact that, in the far wake region when SPCM is active, due to the thrust modulation, there are waves of higher velocity flow traveling downstream, such that the mean flow appears to be "pulsating". This distinctive trait of the PCM-related wake, not studied in the present work, has been preliminary analyzed in Cacciola et al. (2020),[15] showing that it may dramatically affect the downstream turbine aero-servo-elastic response.

A deep inspection of Figure 3 and 4 allows one to further understand the PCM mechanism in relation to the mutual dependency of vorticity and longitudinal streamwise velocity. At second 700 circa, the vortex roll up takes place, compare Figure 3, and an exchange of kinetic energy between in- and out-of-wake regions happens driven by the entrainment of high velocity flow from the outer stream into the wake downstream

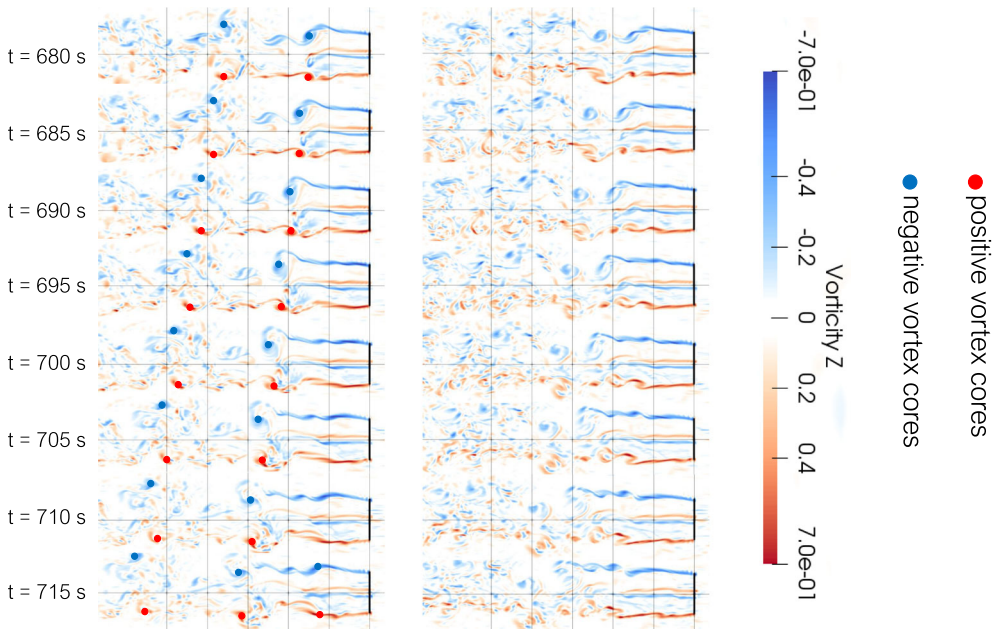

FIGURE 3 Instantaneous vorticity *z* component comparison between standard sinusoidal pitch motion (SPCM) and baseline. Different plots are provided for different time instants (from second 680 to 715) in a time window equal to about one control period

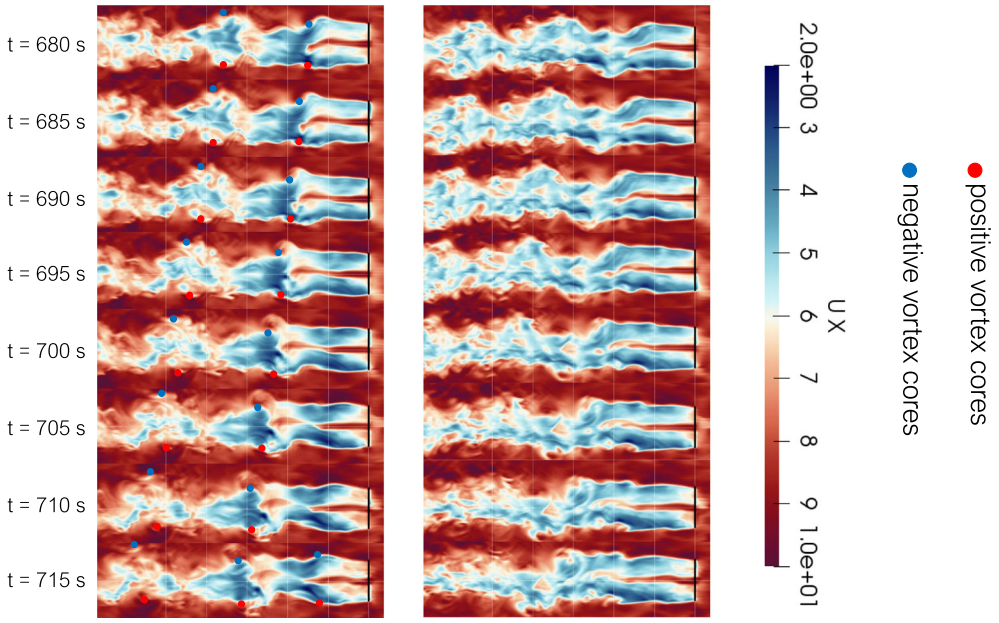

FIGURE 4 Comparison of longitudinal instantaneous velocity component between standard sinusoidal pitch motion (SPCM) (left) and baseline (right). As in Figure 3, different plots are provided for different time instants (from second 680 to 715) in a time window equal to about one control period

the highest vorticity point, as visible in Figure 4. Besides this, low velocity flow from the wake immediately behind the vortex is expelled outside. At this point, the vortex is placed between high speed (downstream) and low speed (upstream) flow; see second 705 and subsequent. This vortex-induced entrainment continues downstream and lasts for several diameters before the vortex is diffused and finally broken by background turbulence. Finally, looking at the baseline case, the entrainment is only due to background turbulence as area of higher vorticity cannot be detected in the in-wake flow.

So far, a fundamental mechanism of the mixing due to PCM has been explained, which consists in the presence of large spatially separated vortex structures, which are advected far downstream before breaking up. The PCM mechanism can be summarized as follows.

- Shear layer zone (0–1.5 *D*): pulsating flow are shed by rotor. Maximum wake velocity defects are located in correspondence of their vorticity peaks. A velocity directed towards wake centerline is induced on the flow immediately downstream this point, while the opposite happens upstream.
- Vortex roll up (1.5–2.5 *D*): shear layers roll up around their maximum vorticity point. High momentum flow starts to be entrained downstream.
- Induction zone (2.5–5 *D*): vortices move downstream while entrainment from outer flow continues. As vortices are advected, they become more diffused.
- Conventional far wake (>5-6 *D*): PCM vortices dissolve and small-scale turbulence provides for the conventional wake re-energization process.

Obviously, such mechanism can be influenced by a suitable choice of the PCM time history, which is able to promote and encourage the vortex roll up. For example, increasing the positive peak of the PCM function would entail in sequence an increase in the pitch angle, a reduction of the blade sectional angles of attack and lift, which approach very low values, and finally, a strong reduction of the associated tip vortices. As a matter of fact, the spatial separation between the high vorticity regions, associated to the lowest pitch values, results higher, easing their roll up.

For purely single frequency sinusoidal PCM, increasing the value of the positive peak necessarily yields a negative peak of equal entity, which may be detrimental in terms of blade loading and PCM effectiveness, being associated to higher blade sectional angle of attack, possibly in the post-stall region.

Now, it is possible to understand the rationale behind the use of a nonsymmetric GPCM as defined in Section 2.3.3. GPCM function, in fact, showing a prominent positive peak and a rather limited negative one, is designed in order to encourage those fluid dynamics phenomena underlying in-wake mixing, as discussed above. Clearly, also, GPCM is a zero mean function, and therefore, it is expected not to significantly influence the turbine trim.

The improvement due to GPCM can be demonstrated through LES simulations as well. Figure 5 reports two time shots of the vorticity measured in a horizontal slice at hub height. The figure refers to the instant associated to the complete shear layer roll up, which happens at around 1.5 diameters in the case of GPCM (bottom plot) and at 2.5 diameters in the SPCM case (upper plot). From this observation, one may imagine that

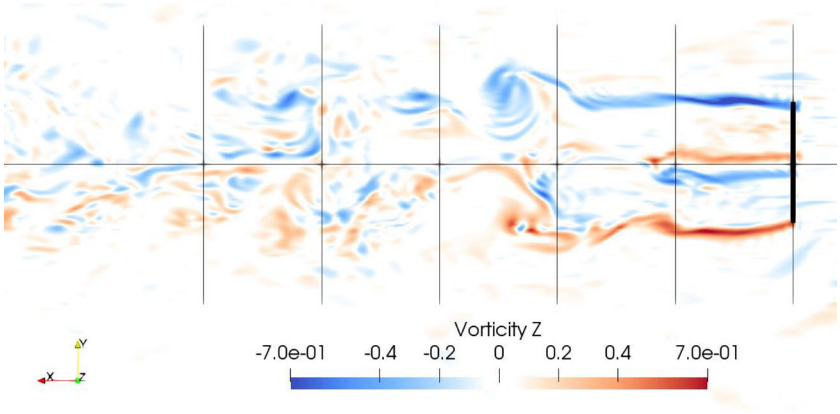

(A) SPCM strategy

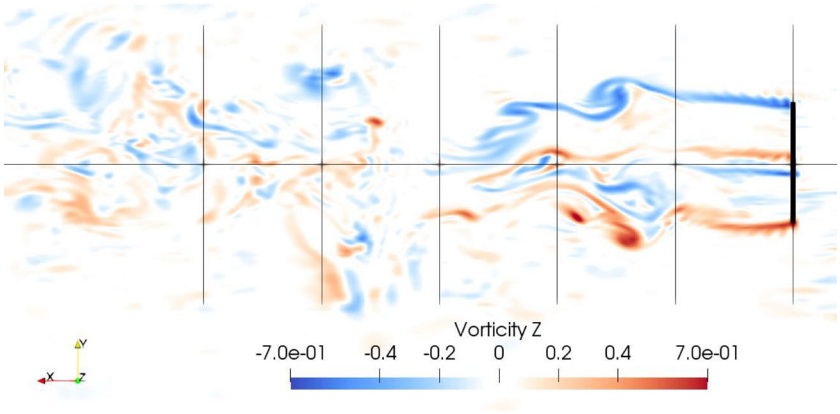

(B) GPCM strategy

FIGURE 5 (A, B) Vorticity plot at the instant of vortex roll up. Comparison between standard sinusoidal pitch motion (SPCM) (upper plot) and Gaussian PCM (GPCM) (bottom plot) cases

GPCM could be more effective than SPCM because the former forces the entrainment process to start closer to the upstream rotor. This particular fact will be demonstrated through two-turbine wind farm simulations in Section 4.2.

Figure 6 shows the 3D snapshot of 0.03 Q-criterion contours colored with velocity magnitude for GPCM (left) and baseline (right) cases. Coherent and lasting structures are clearly visible only in the PCM case, while the baseline case is characterized by simple turbulence-induced mixing. A similar plot, not shown here for the sake of brevity, can be derived also for the SPCM case.

3.2 | Impact of blade tip deflection on near wake vortices

At this point of the treatment, a question may arise over the possibility of improving the PCM strategy through alternative techniques. In fact, due to their prominent role in the wake mixing mechanism, it could be conceivable to directly modify the development of tip vortices through a localized action in the place where they are actually released into the flow, that is, the outermost blade part. If this strategy proved effective, it would have the advantage of having a minor actuation cost and possibly minor impact on wind turbine loading. To this end, the blade was equipped with a movable tip with length equal to 10% of the blade and the sinusoidal PCM function was then apply only to that part. This strategy was named tip PCM or TPCM (cf. Section 2.3.3). The effect of TPCM on the wake is now analyzed.

As written at the beginning of Section 3, the vortex filaments, released by blade tips, separate the wake from the outer flow preventing the exchange of energy. The early breaking of these structures is associated to an improved in-wake mixing. Consequently, studying how long such a shielding effect lasts can provide one with a qualitative information on the control strategy effectiveness.

To this end, the average vorticity over three PCM periods has been calculated and plotted with a threshold color map. Figure 7 shows the average vorticity in a plane parallel to the ground at the hub height in the first two diameters downstream. Along with the baseline case displayed

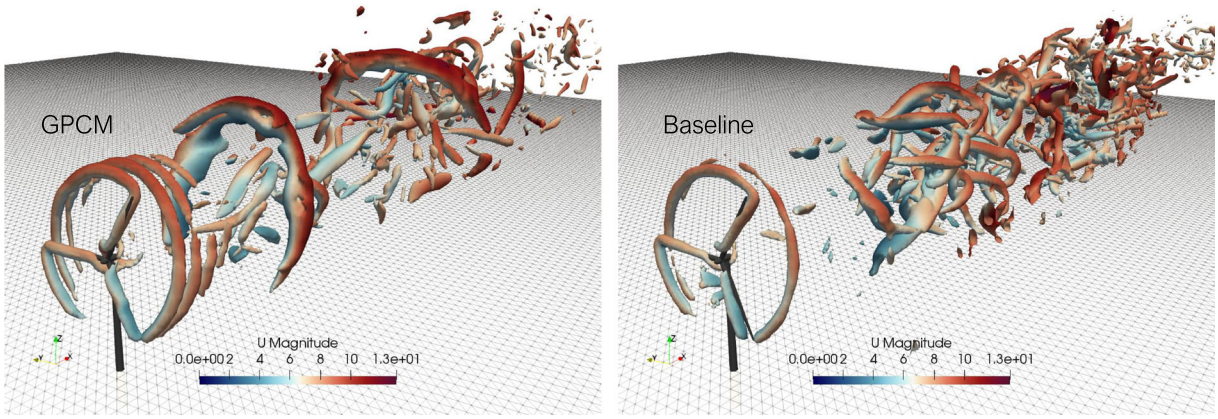

FIGURE 6 The 3D Q-criterion contours comparison between Gaussian PCM (GPCM) (left) and baseline (right)

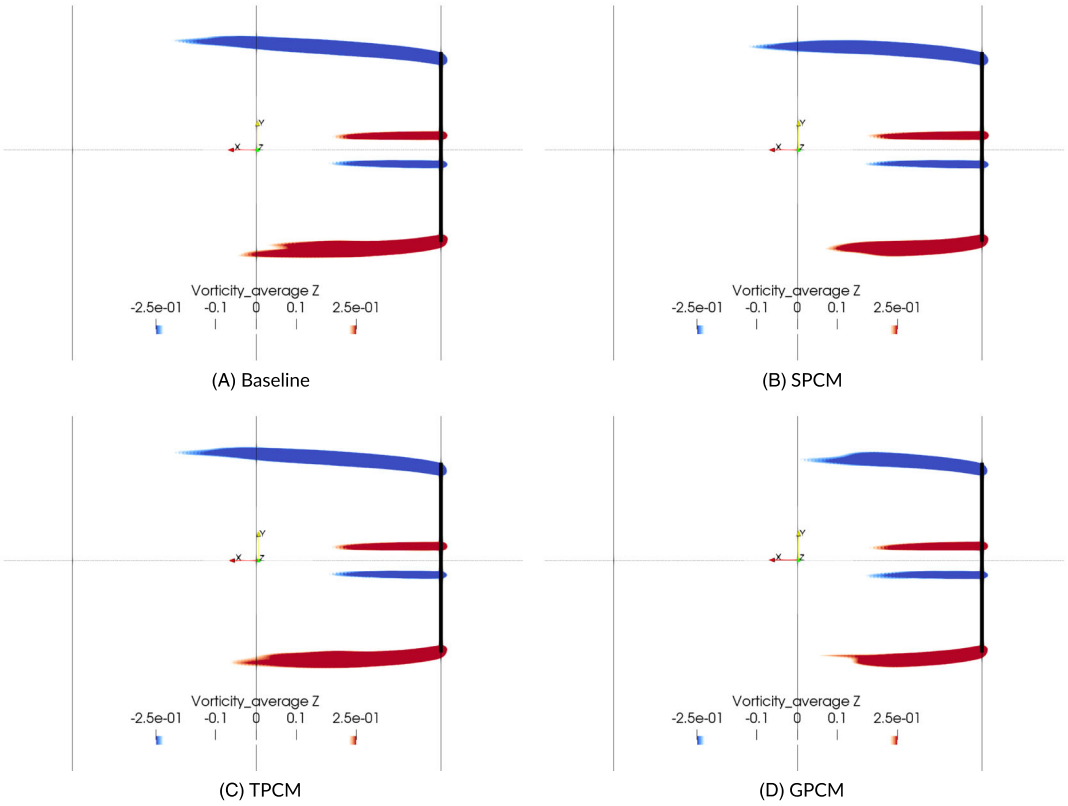

FIGURE 7 (A–D) Comparison of vortex shielding reduction among periodic collective motion (PCM) methods. Top-left plot: baseline case without dynamic induction control (DIC); top-right plot: standard sinusoidal pitch motion (SPCM); bottom-left plot: tip PCM (TPCM); bottom-right plot: Gaussian PCM (GPCM)

in the up-left plot, all PCM strategies are reported, that is, the SPCM in the up-right plot, the TPCM in the bottom-left plot, and the GPCM in the remaining position. Clearly, the highest shielding reduction is given by GPCM, while TPCM does not provide any significant effect with respect to the baseline case.

The reason of the apparent ineffectiveness of the TPCM lays in the fact that the vorticity released into the wake depends on the variation of lift both in time and along the blade, Consequently, a modification of the lift of a limited part of the blade, although localized in a region of particular interest for vorticity generation, cannot entail that significant variation of thrust and vorticity that is able to trigger adequately the in-wake mixing mechanism.

4 | EFFECTIVENESS OF PROPOSED DIC TECHNIQUES

Following the analysis on the physics of the DIC, the present section deals with a quantitative evaluation of the three PCM strategies. The results present in this section consider first the isolated turbine case to evaluate the impact of PCM on the velocity fields. Then, simple two-turbine cases are presented in order to evaluate the farm power production and its dependency on turbulence intensity and longitudinal spacing.

4.1 | Single-turbine wake

The CFD simulation environment in the case of single turbine is the same described in Section 2, which was also used for the analysis already presented in Section 3. The longitudinal flow behind the turbine was recorded and analyzed for the baseline scenario as well as for the three different PCM techniques considered. The vertical profile of the in-wake flow is first analyzed. The successor simulation case refers to the ABL precursor indicated with named P-Z003 (see Table 1), with mean speed of 9 m/s and TI of 5%. Figure 8 shows the nondimensional velocity profile averaged over 10 PCM periods, for baseline "B-Z003", SPCM "S-Z003", GPCM "G-Z003", and TPCM "T-Z003" cases. Different downstream positions are considered in the subplots as indicated in the related captions. Two dash-dotted black horizontal lines indicate the upper and lower position of the rotor blade tip.

Two main considerations can be derived. First, notice that the TPCM, as expected from the previous analyses, does not provide significant benefits in terms of in-wake velocity increase, as the baseline, and TPCM curves are practically indistinguishable for all downstream locations.

Second, both SPCM and GPCM strategies are responsible for an increase in the mean flow velocity, with the latter being more effective especially at 3 *D* downstream. This last observation had been actually foreseen, looking at the vorticity fields shown in Figure 5 and the difference in the downstream position at which the vortex roll up occurs.

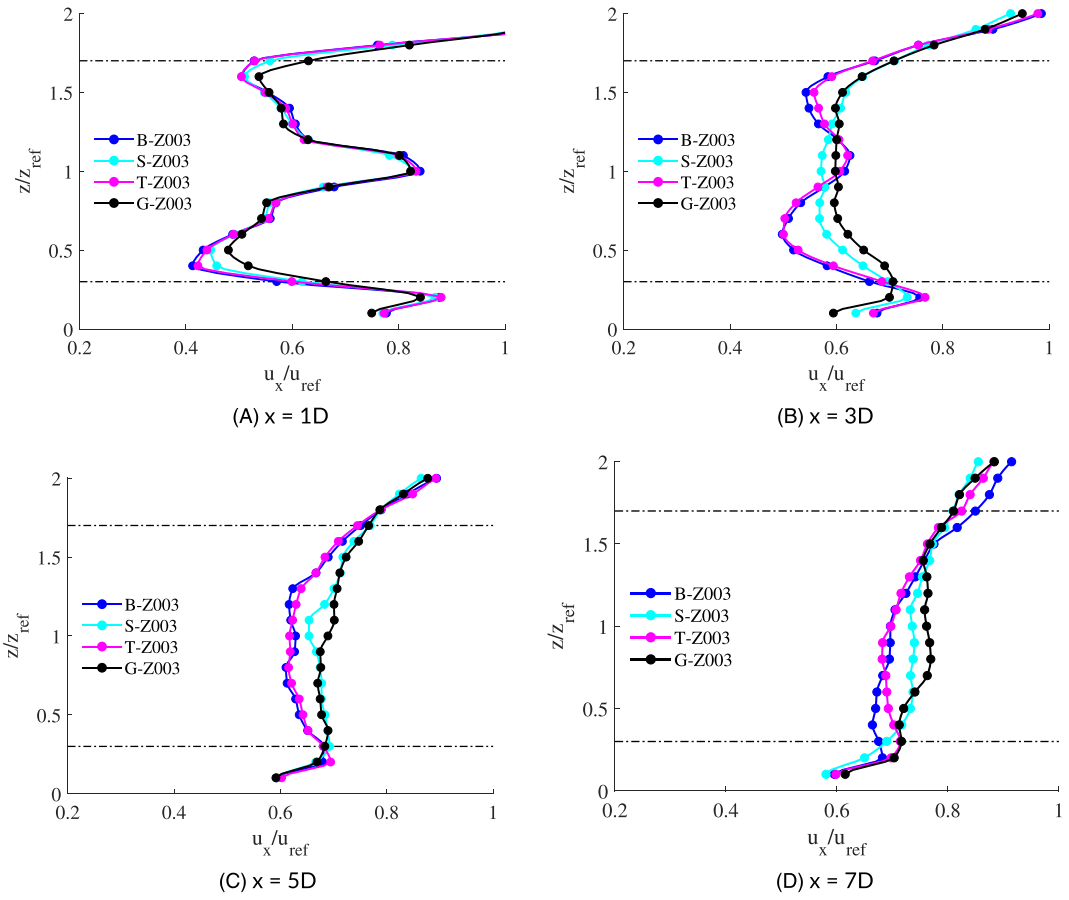

FIGURE 8 (A–D) Nondimensional vertical velocity profile on the turbine symmetry plane averaged over 10 dynamic induction control (DIC) periods, for an ABL with hub height speed 9 m/s and $z_0 = 0.03$. Downstream distance (from 1 to 7 *D*) is indicated in subplot captions. "B-Z003": baseline; "S-Z003": SPCM; "T-Z003": GPCM; "T-Z003": TPCM

The downstream flow velocity at each point of several cross sectional slices was also averaged over 10 PCM periods, then, the averaged values of baseline and PCM strategies have been compared. The percentage gain of SPCM and GPCM techniques with respect to the baseline case is depicted in Figure 9. The plots on the left column represent the gains obtained with the SPCM for different downstream position as indicated by the subplot captions. Similarly, the right column deals with the same results for the GPCM case. The purple circle indicates the position of the rotor disk.

Clearly, both GPCM and SPCM techniques can produce an increase in the in-wake flow velocity, particularly visible from 3 *D*. At 7 *D* the benefit of PCM still persists even if with a lower magnitude. As described in the previous analyses, the GPCM appear to be more effective than the SPCM at lower downstream distances, that is, between 1 and 3 *D*.

A similar analysis, not shown here for the sake of brevity, was performed also for TPC, showing once again its ineffectiveness to increase the wake velocity.

Finally, the arithmetic average of the sectional velocity has been computed over the rotor disk, so as to have a more concise indication of the effectiveness of the proposed PCM techniques.

Figure 10 displays the sectional velocity as function of different downstream positions for baseline and PCM techniques. The velocity, in the *y*-axis, is normalized with respect to the undisturbed flow velocity, whereas distance in the *x*-axis normalized with the rotor diameter.

Blue line, indicated with "B-Z003", shows how the wake velocity recovers from 1 to 7 *D* without PCM. The purple line, indicated with "T-Z003", refers to the TPCM and shows once again the lack of effectiveness of this strategy. Black and light blue lines refer, respectively, to GPCM ("G-Z003") and SPCM ("S-Z003"). Although a faster wake recovery can be observed for both controls, the former exhibits stronger velocity increments in the near wake (1 to 3 diameters), reaching a maximum mean velocity module percentage gain with respect to the baseline of 14% at 3 *D*. The SPCM strategy at the same distance produces a gain equal to about 8%. The larger value associated to GPCM is due to a very effective tip vortices recombination, which leads to stronger re-energization in the near wake region (see Section 3).

4.2 | Two-turbine wind farm

In the present section, results from simple two-turbine farm analyses are presented. The simulations consider both SPCM and GPCM techniques, excluding the tip PCM, which proved ineffective as reported in the previous analyses.

The performance indicator, selected in order to evaluate the improvement of the PCM strategies, is the power of the overall farm, which is analyzed as a function of turbine spacing and turbulence intensity.

At first, consider two aligned turbines at a distance equal to 5 *D*. Since the physical presence of a turbine within an air flow modifies also the upstream velocity field, it is appropriate to verify how much the downstream turbine induction affects the flow characteristics between the two turbines and, possibly, the effectiveness of the PCM strategies.

Figure 11 shows the vertical profile of velocity between the two turbines at a distance of 1, 3, 5, and 7*D* from the front one. Specifically, 1*D* and 3*D* distances refer to positions between the two machine, whereas 5*D* exactly corresponds to the position of the downstream machine and 7*D* is behind the second machine. Again, the velocity has been averaged over 10 PCM periods. Baseline, SPCM, and GPCM are considered in this analysis, whereas all simulation cases refer to a condition with mean hub speed equal to 9 m/s and an ABL with $z_0 = 0.003$. By a simple visual inspection, it is possible to assess that both strategies, SPCM and GPCM, entail an increase in the flow velocity with respect to the baseline case, with GPCM being associated to the highest gain, especially at 3 and 5*D*. Moreover, comparing Figure 8 with Figure11, showing the vertical profiles in the same conditions but, respectively, for single-turbine and two-turbine case, one can readily verify that the addition of a second turbine downstream does not significantly modify the effectiveness of GPCM and SPCM strategies in terms of in-wake flow velocity increment up to 5*D*. This suggests that, if downstream turbine does not modify the effectiveness of PCM strategies, the gains in the wake velocity, which are evaluated and studied in Section 4.1 for the single-turbine case, should generate a nonnegligible increment in the power harvested by the downstream turbine. At 5*D* the difference in the velocity gain between the two PCM strategies is reduced, implying that probably a smaller power increment of Gaussian control is to be expected respect to what predicted from single wake analysis in Section 4.1. Finally, at 7*D*, hence, behind the downstream turbine, the PCM re-energization is almost lost. This suggests that probably, in case more turbines are aligned, the sole activation of PCM in the front-row turbines is not sufficient to entail a benefit in the downstream machines from the third row.

Table 2 shows the power harvested by upstream and downstream turbines along with the total farm output and the percentage increase. It is noteworthy that, while the first turbine produces about the same power, a considerable increment is experienced in the second one. In particular, SPCM and GPCM control strategies allow for an overall power gains of 3.0% and 4.1%, respectively. Clearly, the GPCM represents the best option in terms of power production, providing a further gain of 1.1% with respect to the SPCM control. It is expected that for lower spacing than the 5 diameters considered in this case (e.g., 3 or 4*D*) the difference between SPCM and GPCM will be more pronounced. In any case, this advantage is to be viewed in a wider context where also control impacts on turbine design loads are considered. This extremely important topic is beyond the scope of the present paper but is currently under investigation.13

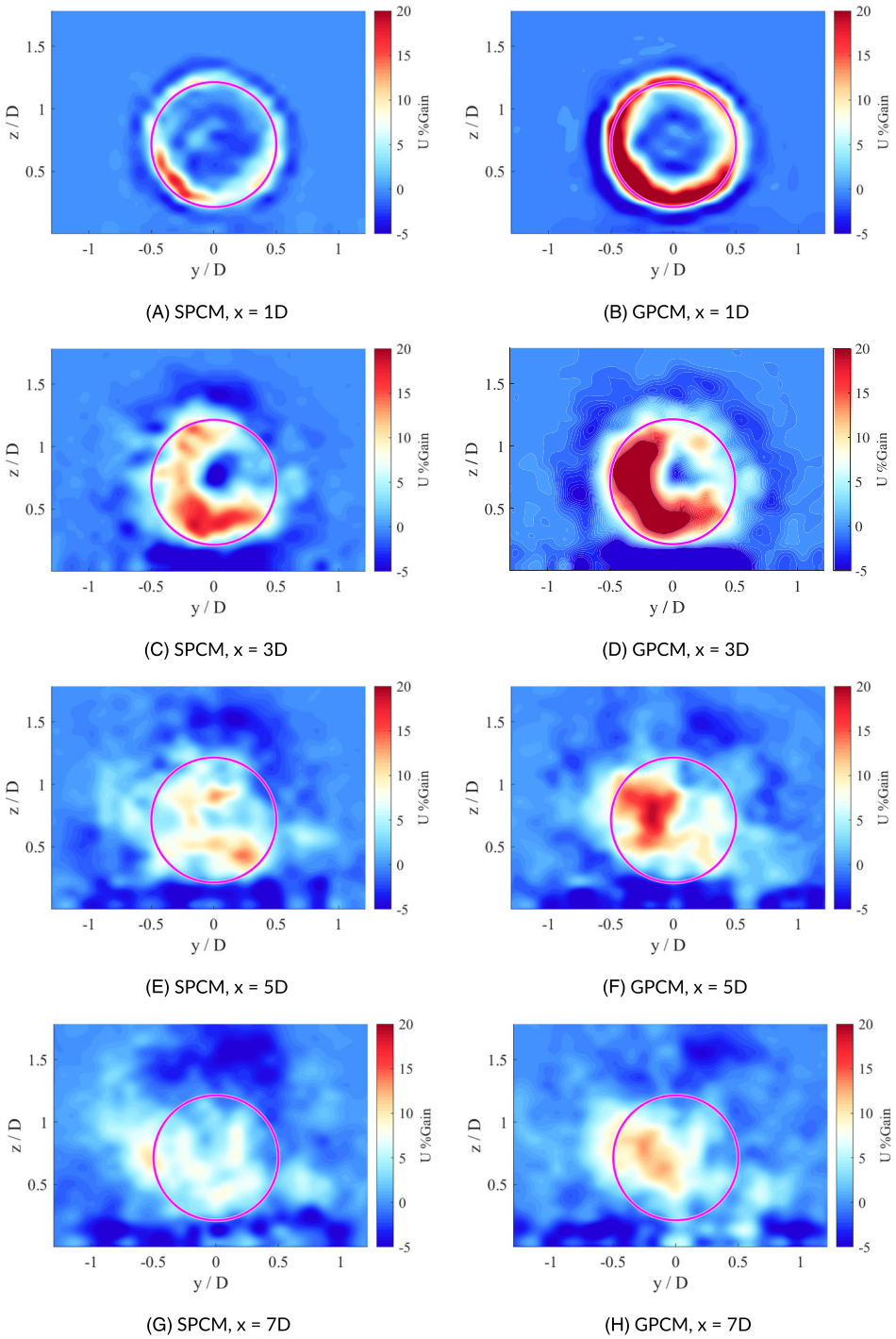

FIGURE 9 (A–D) Streamwise velocity magnitude percentage gain between baseline and SPCM strategy (left column) and between baseline and GPCM strategy (right column). Each row represents a specific downstream section form 1 to 7 *D*. Flow velocity averaged over 10 PCM periods

As suggested by the previous analyses, an additional study has been performed to evaluate the effectiveness of both SPCM and GPCM for different spacing in the case of $z_0 = 0.003$.

Figure 12 shows the gain of the overall power production as function of the turbine spacing, from 3 to 5 *D*. As expected, looking at the impact of GPCM on the wake development in the near wake region (see Sections 3 and 4.1), the gain associated to GPCM is higher than the one of SPCM for low downstream distances. At 3*D*, GPCM entails an increase in the farm power of 7.2%, while SPCM of only 4.6%. The gap between the two strategies progressively lessens as the spacing increases. This result demonstrates that GPCM can be considered a valuable control especially for very low spacing, where also WR is not particularly effective.

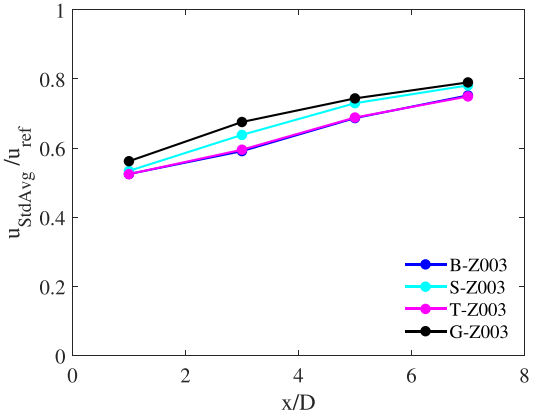

FIGURE 10 Non-dimensional standard average velocity evaluated at x = 1D, x = 3D, x = 5D, and x = 7D

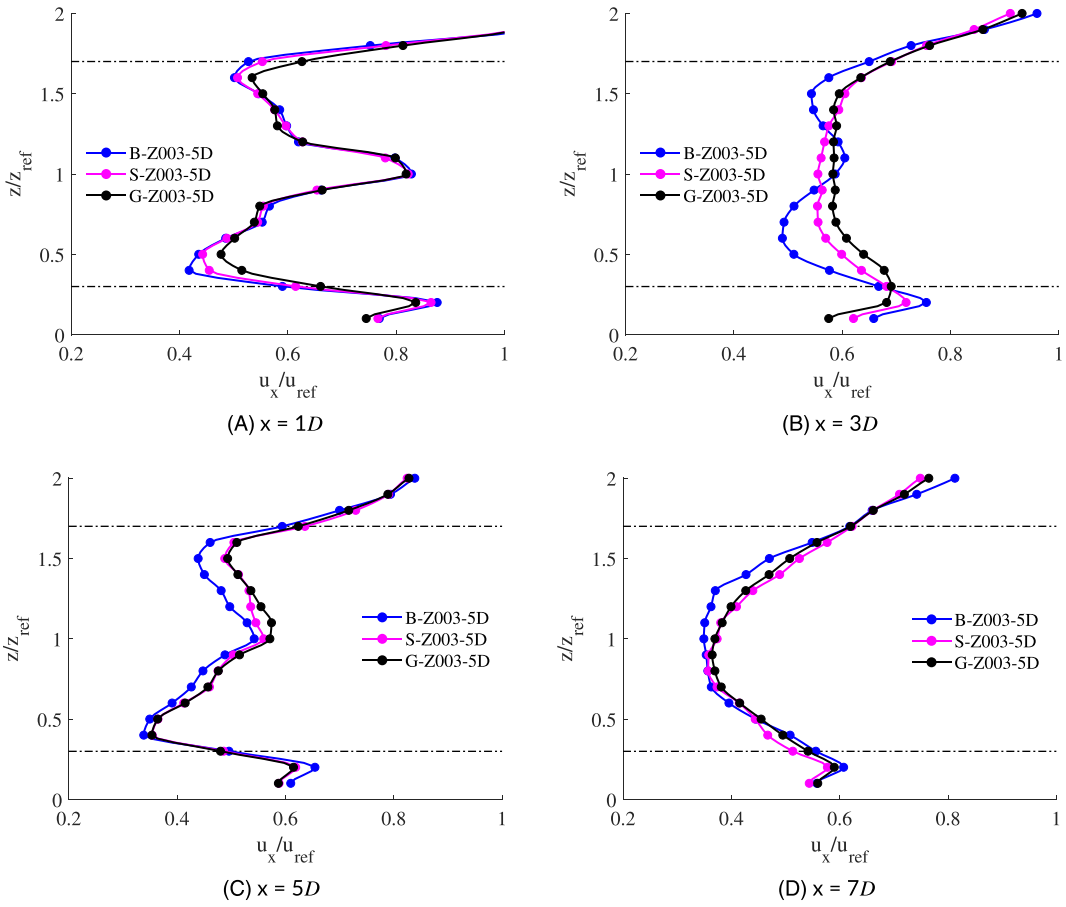

FIGURE 11 (A–D) Nondimensional vertical velocity profile on the turbine symmetry plane averaged over 10 dynamic induction control (DIC) periods, for an ABL with mean hub height speed 9 m/s, $z_0 = 0.003$, in case of two-turbine farm. Baseline: "B-Z003-5D", SPCM: "S-Z003-5D"and GPCM: "G-Z003-5D". Downstream distances are displayed on subfigure captions

4.2.1 | Turbulence intensity influence on overall power production

Due to the in-wake mixing entailed by the background turbulence, wake recovery may be strongly influenced by turbulence intensity. As a consequence, the effectiveness of any wind farm control decreases as TI increases, and possibly may nullify for very high turbulence levels.

In order to evaluate a relationship between DIC and pre-existent ABL turbulence intensity, three different equivalent roughness lengths z_0 has been considered. In particular, the increases in the power output associated to SPCM have been evaluated for $z_0 = 0.003$ responsible for a TI equal to 5.0%, for $z_0 = 0.03$ with TI equal to 6.3% and for $z_0 = 0.15$ with TI equal to 7.3%. Table 3 summarizes the percentage gain of the SPCM

TABLE 2 Overall mean power percentage increase; spacing equal to 5*D*

	Upwind turbine power (kW)	Downwind turbine power (kW)	Farm power (kW)	Total gain
Baseline	2747	1055	3802	(-)
SPCM	2768	1149	3917	3.0
GPCM	2714	1247	3961	4.2

Abbreviations: GPCM, Gaussian PCM; SPCM, standard sinusoidal pitch motion.

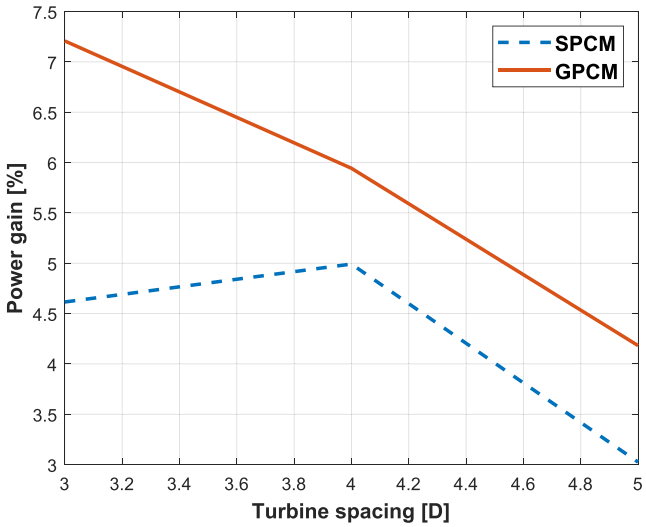

FIGURE 12 Power gain as function of different spacing for standard sinusoidal pitch motion (SPCM), dashed line, and Gaussian PCM (GPCM), solid line

TABLE 3 TI effects on overall mean power gain of the SPCM control over baseline

ABL		Power increase (%)
z_0	TI	
0.003	5.0	4.1
0.030	6.3	3.6
0.150	7.3	4.2

Abbreviations: GPCM, Gaussian PCM; SPCM, standard sinusoidal pitch motion.

over the baseline case as function of the different TI levels. From the obtained results, it is possible to verify that the SPCM entails an almost constant gain of about 4% up to a TI of 7%, but due to the limited range of the explored TI levels, it is difficult to notice a trend in the effectiveness of the control solution. Clearly, additional analyses are needed to define the effectiveness of the controls as function of TI levels.

5 | CONCLUSIONS AND OUTLOOK

The present paper provides a CFD-based analysis on a particular wind farm control technique called DIC. Specifically, DIC is generated by a suitable PCM of the pitch angle (PCM).

The main idea of this study is to analyze from a physical standpoint how the fluid dynamic mechanism underling the wake recovery is boosted by the DIC. Then, thanks to an improved understanding of the DIC working principles, it was possible to propose an innovative PCM strategy, called GPCM. GPCM pitch motion is based on a zero mean asymmetric function with a higher positive peak value, which is tailored to further encourage those fluid dynamics phenomena already exploited by the standard symmetric and sinusoidal PCM (SPCM).

Finally, several simulations with single-turbine and simple two-turbine farm were performed with the goal of evaluating the effectiveness of both GPCM and SPCM, as function of some relevant parameters (i.e., TI and spacing).

From the results obtained in this work, it is possible to derive the following conclusions.

- Since the near wake region is shielded from the outer flow by the organized vortex filaments released from blades, the wake re-energization may take place only after the vortices pair, hence, in the far wake region, where the outer flow can be actually sucked inside the wake. This suggests that a faster wake recovery may be involved by anticipating the entrainment process through an early breaking of the organized vorticity structures.
- When DIC is active, the periodic rotor aerodynamic forces generate, among all, a modulation in the blade tip vortices released in the wake, creating well-separated regions of high vorticity, around which the boundary layer may roll up. The flow rolling up around such high vorticity cores is a significant source of mixing which complements and, in a certain way, boosts the eventual faster wake recovery.
- The wake recovery can be enhanced by promoting such a vortex roll up. This is, in fact, the case of the GPCM, which is characterized by a zero mean asymmetric blade pitch motion with a more prominent positive peak: when the blade pitch setting reaches its highest value, a reduced, almost null, vorticity is released in the wake, promoting this way the flow roll up around the higher vorticity cores, associated to the negative pitch peak.
- From LES analyses, it was possible to prove that GPCM is responsible for an early vortex roll up with respect to the standard SPCM. On the one hand, this justifies a greater potential of the proposed strategy, on the other hand, it demonstrates the correctness of the physical interpretation of DIC working principles which has been derived in this paper.
- Although the tip vortices play a prominent role in the wake recovery process, a PCM action localized where the vortices themselves are shed, that is blade tip, does not seem effective, as demonstrated by the (in)sensitivity of the wake development with respect to the activation of blade tip PCM (TPCM).
- The study of the wake shed by a single wind turbine demonstrates that, up to 5*D*, the percentage gain in mean in-wake velocity associated to GPCM is higher than that of SPCM. Beyond 5*D*, the percentage gains associated to the two controllers are rather similar.
- Considering a simple two-turbine wind farm, both SPCM and GPCM are able to increase the total farm output of some percents. As expected from the analysis of the single wake, the gain depends strongly on the spacing: at 9 m/s and 5*D* both techniques entails and increase of about 4%. For lower spacing, the performance of GPCM results better then the one related to SPCM. As an example at 3*D* the gain associated to GPCM and SPCM are respectively equal to 7% and 4.5%.
- The results of the present analysis were obtained in a simplified scenario (a two-turbine farm with low turbulence level). Clearly, it would be interesting to evaluate how the performance changes if one considers larger farms and higher turbulence levels. It is expected that the effectiveness of all PCM strategies will lessen as the TI increases because the turbulence itself will provide for a significant source of in-wake mixing that may be higher than the one entailed by the PCM control. Additionally, one may expect that, in the case of two or more downstream turbines, the inner machine should also operate according to PCM to significantly improve the overall farm power. In such a case, the effectiveness of the GPCM with respect to the SPCM should be verified especially for the inner machines, that see a flow modified by the presence of the front turbine.

Clearly, this work can be improved in several directions. First, it could be interesting to check whether the presence of the nacelle might modify the effectiveness of PCM and, possibly, quantify such impact. Second, it is certainly important to evaluate farm output gain connected to such controllers for more inflow conditions, including different velocities, higher turbulence intensities, and different shear layers. Third, an analysis on a three-turbine wind farm could lead to interesting results on a more realistic scenario, where the intermediate turbine is subjected to the dynamic wake shed by the upstream one and, at the same time, operates with PCM to entail a faster wake recovery downstream, potentially associated to a power increase in the last machine. Last but not the least, the performance of PCM should be also evaluated for partial wake impingement cases.

In terms of possible extensions of the analysis, verifying the impact of PCM on fatigue and design loads of upstream and downstream machines is a topic of a paramount importance to comprehend the actual potential of PCM to became a valuable farm control for both existing and newly designed wind farms. This particular analyses is currently under investigation.[15]

ACKNOWLEDGEMENT

We acknowledge the CINECA award under the ISCRA initiative, for the availability of high-performance computing resources and support.

AUTHOR CONTRIBUTIONS

Conceptualization, A.C.; methodology, A.C., S.C., and M.M.; software, M.M, R.P., and S.S.; validation, R.P. and S.S.; formal analysis, A.C., S.C., M.M, R.P., and S.S.; investigation, A.C., S.C., M.M., R.P., and S.S.; computational resources, S.C.; data curation, R.P. and S.S.; writing–original draft preparation, S.C. and S.S.; writing–review and editing, A.C.; visualization, R.P. and S.S.; supervision, A.C.; project administration, A.C.; funding acquisition, A.C. All authors have read and agreed to the published version of the manuscript.

CONFLICT OF INTEREST

The authors declare no potential conflict of interests.

PEER REVIEW

The peer review history for this article is available at https://publons.com/publon/10.1002/we.2801.

ORCID

Alessandro Croce https://orcid.org/0000-0002-7640-5253
Stefano Cacciola https://orcid.org/0000-0002-5370-1105

REFERENCES

1. Johnson C, White E, Jones S. Summary of actual vs. predicted wind farm performance recap of windpower 2008. Portland, OR, USA, AWEA Wind Resource Assessment Workshop; 2008.
2. Fleming P, King J, Dykes K, et al. Initial results from a field campaign of wake steering applied at a commercial wind farm – part 1. *Wind Energy Sci*. 2019;4(2):273-285.
3. Gebraad PMO, Teeuwisse FW, van Wingerden JW, Fleming PA, Ruben SD, Marden JR, Pao LY. Wind plant power optimization through yaw control using a parametric model for wake effects CFD simulation study. *Wind Energy*. 2016;19(1):95-114. https://doi.org/10.1002/we.1822
4. Annoni J, Gebraad PM, Scholbrock AK, Fleming P, van Wingerden J-W. Analysis of axial-induction-based wind plant control using an engineering and a high-order wind plant model. *Wind Energy*. 2016;19(6):1135-1150.
5. Munters W, Meyers G. An optimal control framework for dynamic induction control of wind farms and their interaction with the atmospheric boundary layer. *Phil Trans R Soc A: Math, Phys Eng Sci*. 2017;375(2091):20160100-1–19.
6. Goit JP, Meyers J. Optimal control of energy extraction in wind-farm boundary layers. *J Fluid Mech*. 2015;768:50.
7. Goit JP, Munters W, Meyers J. Optimal coordinated control of power extraction in LES of a wind farm with entrance effects. *Energies*. 2016;9(1).
8. Yilmaz AE, Meyers J. Optimal dynamic induction control of a pair of inline wind turbines. *Phys Fluids*. 2018;30(8):85106. https://doi.org/10.1063/1.5038600
9. Gilling L. Tugen: synthetic turbulence generator, manual and user's guide. *Tech Rep* DCE Technical Reports No. 76, Thomas Manns Vej 23, 9220 Aalborg, DK, Department of Civil Engineering, Aalborg University; 2009.
10. Munters W, Meyers J. Dynamic strategies for yaw and induction control of wind farms based on large-eddy simulation and optimization. *Energies*. 2018;11(1):177.
11. Munters W, Meyers G. Towards practical dynamic induction control of wind farms: analysis of optimally controlled wind-farm boundary layers and sinusoidal induction control of first-row turbines. *Wind Energy Sci*. 2018;3(1):409-425.
12. Frederik JA, Weber R, Cacciola S, Campagnolo F, Croce A, Bottasso CL, van Wingerden J-W. Periodic dynamic induction control of wind farms: proving the potential in simulations and wind tunnel experiments. *Wind Energy Sci*. 2020;5(1):245-257.
13. Croce A, Cacciola S, Sartori L. Evaluation of the impact of active wake control techniques on ultimate loads for a 10 mw wind turbine. *Wind Energy Sci*. 2022;7:1-17.
14. Wang C, Campagnolo F, Sharma A, Bottasso CL. Effects of dynamic induction control on power and loads, by les-alm simulations and wind tunnel experiments. *J Phys: Confer Ser*. 2020;1618(2):22036-1–8.
15. Cacciola S, Bertozzi A, Sartori L, Croce A. On the dynamic response of a pitch/torque controlled wind turbine in a pulsating dynamic wake. *J Phys: Confer Ser*. 2020;1618(6):62033-1–10.
16. Frederik JA, Doekemeijer BM, Mulders SP, van Wingerden J-W. The helix approach: Using dynamic individual pitch control to enhance wake mixing in wind farms. *Wind Energy*. 2020;23(8):1739-1751. https://doi.org/10.1002/we.2513
17. Frederik J, Doekemeijer B, Mulders S, van Wingerden J-W. On wind farm wake mixing strategies using dynamic individual pitch control. *J Phys: Confer Ser*. 2020;1618(2):22050-1–9. https://doi.org/10.1088/1742-6596/1618/2/022050
18. Jonkman JM, Buhl LJ. Fast user's guide. *Tech Rep* NREL/EL-500-38230, National Renewable Energy Laboratory (NREL); 2005.
19. Churchfield M, Lee S. Nwtc design codes-SOWFA. *Tech Rep*, National Renewable Energy Laboratory (NREL); 2012. http://wind.nrel.gov/designcodes/simulators/SOWFA
20. Churchfield MJ, Schreck SJ, Martinez LA, Meneveau C, Spalart PR. An advanced actuator line method for wind energy applications and beyond. In: 35th Wind Energy Symposium; 2017.
21. CINECA. Hpc high power computing. https://www.hpc.cineca.it/; 2022.
22. Rampanelli G, Zardi D. A method to determine the capping inversion of the convective boundary layer. *J Appl Meteorol*. 2004;43(6):925-933.
23. Brasseur JG, Wei T. Designing large-eddy simulation of the turbulent boundary layer to capture law-of-the-wall scaling. *Phys Fluids*. 2010;22(2):21303.
24. Schumann U. Subgrid scale model for finite difference simulations of turbulent flows in plane channels and annuli. *J Comput Phys*. 1975;18:376-404.
25. Moeng C-H. A large-eddy-simulation model for the study of planetary boundary-layer turbulence. *J Atmosp Sci*. 1984;41(13):2052-2062.
26. Paulson CA. The mathematical representation of wind speed and temperature profiles in the unstable atmospheric surface layer. *J Appl Meteorol*. 1970;9(6):857-861.
27. Jonkman J, Butterfield S, Musial W, Scott G. Definition of a 5-mw reference wind turbine for offshore system development. *Tech Rep* TP-500-38060, Golden, CO, USA, National Renewable Energy Labpratory (NREL); 2009.
28. Lignarolo LE, Ragni D, Simao Ferreira C, van Bussel GG. Experimental quantification of the entrainment of kinetic energy and production of turbulence in the wake of a wind turbine with particle image velocimetry. In: 32nd ASME Wind Energy Symposium; 2014.
29. Wu Y-T, Porté-Agel F. Atmospheric turbulence effects on wind-turbine wakes: An les study. *Energies*. 2012;5:5340-5362.

30. Porté-Agel F, Bastankhah M, Shamsoddin S. Wind-turbine and wind-farm flows: a review. *Bound-Layer Meteorol*. 2020;174(1):1-59.
31. Medici D. Experimental studies of wind turbine wakes: power optimisation and meandering. *Ph.D. Thesis*: KTH; 2005.
32. Felli M, Camussi R, Di Felice F. Mechanisms of evolution of the propeller wake in the transition and far fields. *J Fluid Mech*. 2011;682:5-53.

How to cite this article: Croce A, Cacciola S, Montero Montenegro M, Stipa S, Praticó R. A CFD-based analysis of dynamic induction techniques for wind farm control applications. *Wind Energy*. 2022;1-19. doi:10.1002/we.2801